DOI: 10.1002/adma.202312856
**Article type: Research Article**

# Antiferroelectric Ceramics for Energy-Efficient Capacitors by Theory-Guided Discovery

*Anand P.S. Gaur, Renu Choudhary, Binzhi Liu, Yaroslav Mudryk, Duane D. Johnson, Jun Cui and Xiaoli Tan**

Dr. A. Gaur, Dr. R. Choudhary, Dr. B. Liu, Prof. D.D. Johnson, Prof. J. Cui, Prof. X. Tan
Department of Materials Science and Engineering, Iowa State University, Ames, IA 50011, USA
*E-mail: xtan@iastate.edu

Dr. Y. Mudryk
U.S. DOE Ames National Laboratory, Ames, IA 50011, USA

**Abstract.** Antiferroelectric ceramics, via the electric-field-induced antiferroelectric (AFE) – ferroelectric (FE) phase transitions, show great promise for high-energy-density capacitors. Yet, currently, only 70~80% energy release is found during a charge-discharge cycle. Here, for $PbZrO_3$-based oxides, we apply geometric nonlinear theory of martensitic phase transitions (first used to guide supercompatible shape-memory alloys) to predict the reversibility of the AFE–FE transition by using density-functional theory to assess AFE/FE interfacial lattice-mismatch strain that assures ultralow electric hysteresis and extended fatigue lifetime. We observe a good correlation of mismatch strain with electric hysteresis, hence, with energy efficiency of AFE capacitors. Guided by theory, we conduct high-throughput materials search and discover AFE compositions with a near-perfect charge-discharge energy efficiency (98.2%), i.e., near-zero hysteresis. And the fatigue life of the capacitor reaches 79.5 million charge-discharge cycles, a factor of 80 enhancement over AFE ceramics with large electric hysteresis.

**Keywords**: antiferroelectric – ferroelectric phase transition, geometric nonlinear theory of martensite, lattice-mismatch strain, electric hysteresis, energy efficiency, $PbZrO_3$-based oxides

## 1. Introduction

Capacitors are used in virtually all electronic devices and are ubiquitous in human life. For instance, every smartphone has ~1,000 capacitors and every inverter in an electric car needs a DC-link with huge capacitance (~1,000 mF).[1] Ceramic capacitors account for ~90% of the market by volume, with more than three trillion multilayer ceramic capacitors manufactured each year.[2,3] Capacitors with a high energy density and high efficiency are critical components in computers, cell phones, medical devices and in the power electronics for motor drives, solar voltaic, wind energy, and power grid.[3-5]

AFE ceramics (like $PbZrO_3$-based) stand out from dielectrics for high energy-density capacitors due to the electric field-induced AFE–FE phase transition.[6-10] As shown in the polarization ($P$) vs. electric field ($E$) diagram in **Fig. 1a**, the AFE phase transforms to the FE phase at the field $E_F$ during charging, storing an amount of energy (per volume) quantified as $W_{st} = \int_0^{P_{max}} EdP$; during discharge, the reverse transition occurs at field $E_A$ with the recoverable energy (per volume) expressed as $W_{rec} = \int_{P_r}^{P_{max}} EdP$, where $P_{max}$ and $P_r$ are polarizations at the peak and zero fields, respectively. The charge-discharge energy efficiency of a dielectric capacitor is assessed according to $\eta = W_{rec}/W_{st}$. In addition to their high $W_{rec}$ values, AFE capacitors can achieve a discharge rate 100× faster than batteries, allowing excellent power density.[1,4,11,12] These outstanding features make AFE capacitors ideal for systems requiring high frequency (1~100 kHz) power conditioning and fast discharge (<1 μs) pulse power.

However, despite their high energy density and powder density, AFE capacitors are barely commercially available.[13] The main limiting factor is the short charge-discharge cycle lifetime ($N_f$ ~1 million cycles) resulting from the large electric hysteresis $\Delta E$ of the AFE–FE phase transition.[14,15] Furthermore, as evident from **Fig. 1a**, a large $\Delta E$ corresponds to a low energy efficiency $\eta$, reported in the range of 70~80% in most $PbZrO_3$-based[11,16-19] and

below 70% in most Pb-free AFE ceramics.[3,20] A considerable amount of energy is then converted to heat and wasted. This is detrimental to AFE devices especially for their niche applications at high frequencies. Therefore, AFE ceramics with minimum $\Delta E$ are highly desirable as they are expected to have an extended charge-discharge service lifetime.[21-24] In recent years, a trial-and-error empirical approach has been employed and $PbZrO_3$-based compositions with $\eta > 90\%$ have been identified.[25-28] But the theory that can guide the development of AFE materials with minimum $\Delta E$ and ultrahigh $\eta$ is still lacking.

Microstructurally, the AFE–FE phase transition is accomplished through the motion of the AFE/FE interface.[29] We suggest that the incompatible interface nature (unmatched AFE and FE lattice interface and abruptly terminating polarizations) is the origin for the large $\Delta E$, hence, the mediocre $\eta$, and limited $N_f$. Incompatible AFE/FE interfaces possess elastic distortion and electrostatic energies, resulting in low interface-mobility and poor phase-transition-reversibility. The AFE–FE phase transition is displacive, resembling the austenite–martensite transition in shape-memory alloys. The geometric nonlinear theory of martensite was developed to describe the effect of the crystalline lattice mismatch on austenite–martensite phase transition hysteresis and fatigue life.[30-32] It was experimentally validated and utilized to drastically improve the reversibility of martensitic transitions in shape-memory alloys.[33-35] Attempts have been recently made to extend this theory to oxide ceramics.[36-38] Here, we demonstrate the use of geometric nonlinear theory of martensitic transition to guide the AFE – FE phase transition interfacial mismatch in $PbZrO_3$-based oxides and achieve a charge-discharge energy efficiency of 98.2%, a world record for AFE ceramics.

## 2. Results and Discussion

**Figure 1b** shows the $P$ vs. $E$ curve of the $(Pb_{0.87}Sr_{0.05}Ba_{0.05}La_{0.02})(Zr_{0.52}Sn_{0.40}Ti_{0.08})O_3$ ceramic (abbreviated as SB5408), a $PbZrO_3$-based AFE ceramic we discovered with a record-

high efficiency $\eta$=98.2% with energy density $W_{rec}$=3.0 J/cm$^3$ at 220 kV/cm of applied field. Based on our hypothesis, the nearly hysteresis-free $P$ vs. $E$ curve in SB5408 is a manifestation of its highly compatible and mobile AFE/FE interfaces. The highly reversible AFE–FE transition engenders a strong fatigue resistance to the ceramic, surviving a record-long $7.95\times10^7$ charge-discharge cycles with only 5.8% reduction in $P_{max}$ (**Fig. 1c**). The $P_r$ remains low at 0.4 μC/cm$^2$ after fatigue. Most importantly, $\eta$ remains almost unchanged (a 1.5% loss) and $W_{rec}$ retains 91.3% of its initial value. Compared against other AFE bulk ceramics reported, our ceramics discovered by theory-guidance exhibit the highest energy efficiency (**Fig. 1d**) and the longest endurance, particularly promising for high-frequency applications.

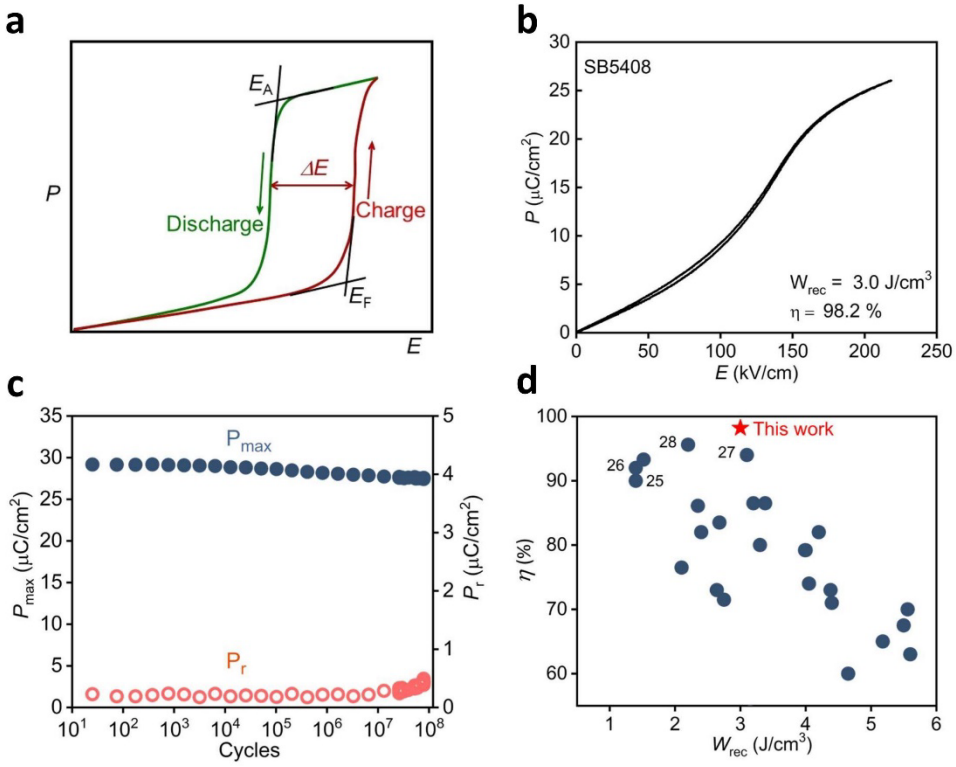


**Figure 1.** AFE ceramics with record-high energy efficiency and fatigue endurance. **a**. Schematic unipolar $P$ vs. $E$ hysteresis loop of typical AFE ceramics showing $E_F$, $E_A$, and electric hysteresis $\Delta E$. **b**. The $P$ vs. $E$ curve measured at room temperature under a unipolar field of 220 kV/cm in the ceramic of SB5408. **c.** The evolution of $P_{max}$ and $P_r$ during fatigue test. **d**. Comparison of the ceramic SB5408 against other $PbZrO_3$-based AFE bulk ceramics for their $\eta$ and $W_{rec}$ reported in the literature; the ceramics with the highest $\eta$ are reported in Ref. 25-28, those with lower $\eta$ values are taken from Ref. 3.

Our $PbZrO_3$-based AFE ceramics with near-perfect energy efficiencies are discovered by density-functional theory (DFT)-guided geometric nonlinear theory of AFE–FE transition (Details are provided in Supplementary Information and **Fig. S1**). Based on previous empirical studies,[11,21,22] the (Pb,Sr,Ba,La)(Zr,Sn,Ti)$O_3$ solid solution was used as the model system. We conducted preliminary tests and confirmed the benefits of doping elements Sr, Ba, and Sn on reducing electric hysteresis (**Fig. S2**). **Figure 2a** shows the composition space of the B-site elements (Zr, Sn, Ti) in our investigation. In addition, we also included Sr, Ba, and La substitution on the A-site in our calculations.

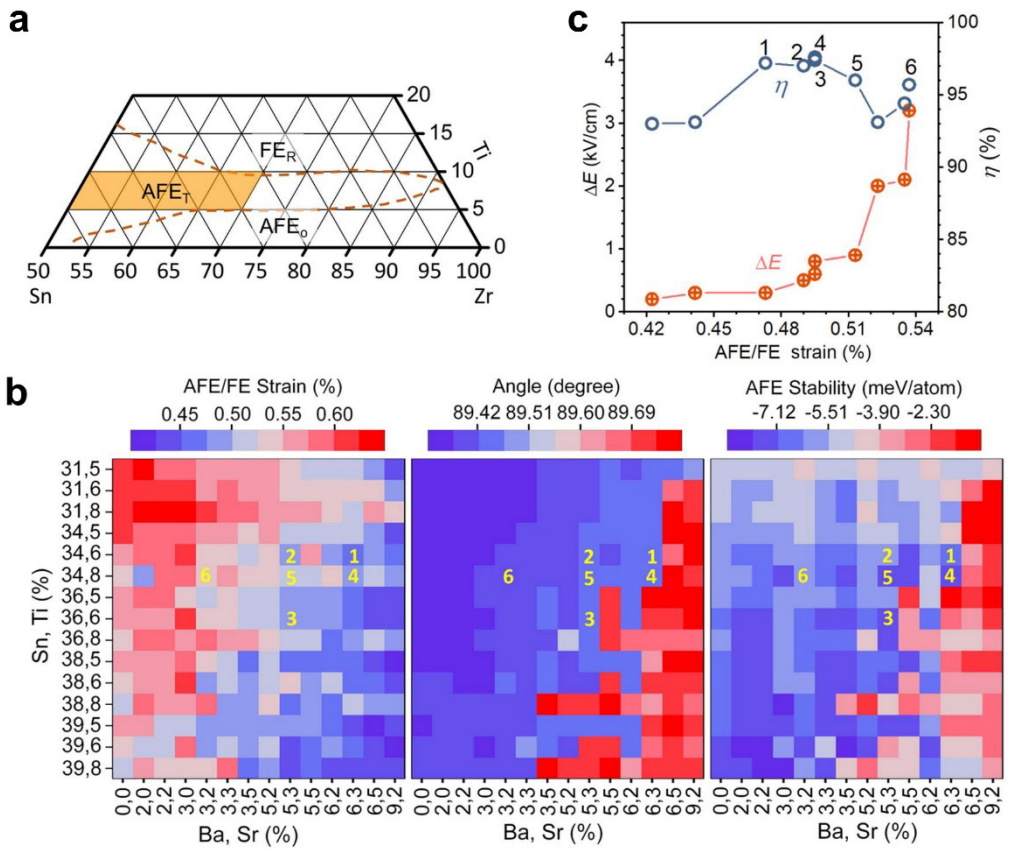


**Figure 2.** Theory predictions of energy-efficient AFE ceramics and their experimental validations. **a**. Ternary phase diagram of $(Pb_{0.97}La_{0.02})(Zr,Sn,Ti)O_3$ (from Ref. 11) where orthorhombic AFE ($AFE_O$), tetragonal AFE ($AFE_T$), and rhombohedral FE ($FE_R$) phases are delineated. The composition space of B-site cations in the theoretical calculations is denoted by orange shading. **b**. Color heat maps (from left to right) display the calculated AFE/FE mismatch strain, FE-cell distortion angle ($\neq 90^o$), and the AFE stability, respectively, in compositions with varying contents of Ba/Sr on A-sites and Sn/Ti on B-sites. **c**. Experimental validations of theory down-selected 10 compositions for their $\Delta E$ and $\eta$ with respect to the calculated AFE/FE strains. Six of them exhibit an $\eta > 95.0\%$, with their compositions marked in **b**. The La-content is 3 at.% in compositions displayed in **b** and **c**.

The geometric nonlinear theory of martensitic transform specifies conditions: (i) *det* **U** = $\lambda_1\lambda_2\lambda_3 = 1$ (percent volume change), and (ii) $\lambda_2 = 1$ (ideal compatibility) to have a compatible interface between the transient phases.[33,34] Here **U** is the transformation stretch tensor that maps the martensite lattice to the austenite lattice, *det* **U** is its determinant; and $\lambda_1 \leq \lambda_2 \leq \lambda_3$ are the ordered eigenvalues of **U**.[33] The DFT calculations of crystal structures and quantification of *det* **U** and $\lambda_2$ have been provided in the Supplementary Information. Experimentally, in shape-memory alloys, the second condition ($\lambda_2 = 1$) was shown to be sufficient to achieve compatibility at the austenite/martensite interface.[33] Thus, in our high-throughput DFT results, we focused on calculating the $\lambda_2$ value for (Pb,Sr,Ba,La)(Zr,Sn,Ti)$O_3$ compositions by optimizing their structures in AFE and FE phases, where we monitor $|1- \lambda_2|$ as an indicator of the AFE/FE mismatch strain, which should approach zero for a compatible interface. Notably, to make faster theory estimates (and avoid very large supercells), we assumed that ideal AFE and FE crystals could be addressed by applying algebraically the **U** stretch tensor to monitor compatibility between AFE and FE structures.

We first calculated $|1- \lambda_2|$ in four composition series, each has only one varying element content. Selected compositions within these series were fabricated into ceramics and their electric hysteresis $\Delta E$ were experimentally determined. As shown in **Fig. S2**, an excellent agreement between AFE/FE strain and $\Delta E$ is found: a lower AFE/FE strain corresponds to a smaller $\Delta E$. We then expanded our high-throughput results to a large composition space by simultaneously varying contents of Sr, Ba, Sn, and Ti (**Fig. 2b**). In addition to the AFE/FE mismatch strain, we also mapped out the distortion angle of the FE rhombohedral phase primitive cell and the energy difference between the AFE and FE phases. As a rapid measure, we validated that the FE-cell angle correlates well with experimentally determined $P_{max}$ (deviations from 90° correlate to a larger $P_{max}$, see **Fig. S3**). The DFT energy difference between AFE and FE phases indicates the relative AFE phase stability, hence, reflects $E_F$ of the composition. A larger absolute value of the calculated AFE stability indicates that the

AFE phase is more stable, and a higher $E_F$ is needed to trigger the AFE to FE transition. The FE-cell angle and AFE stability are critical factors dictating the energy density of the ceramic.

For AFE capacitors, a near-perfect $\eta$ and a large $W_{rec}$ are desired. Practically, $E_F$ needs to be high, but is limited by the dielectric breakdown strength of the ceramic. Therefore, compositions would perform best with a low AFE/FE strain, a small FE-cell angle, and a medium AFE stability from DFT results. **Figure 2b** clearly shows that these are conflicting requirements: compositions with good compatibility (high in $\eta$) are often low in both $P_{max}$ and $E_F$ (low $W_{rec}$). We set the selection criteria of AFE/FE strain ≤ 0.54%, FE-cell angle in the range of 89.40° ~ 89.50°, and AFE-stability in the range of -6.0 to -7.5 meV/atom to identify the best predicted compositions.

The DFT-predicted "best" 10 compositions were all experimentally fabricated and tested. The experimental results on $\Delta E$ and $\eta$ are plotted against the theoretically calculated AFE/FE strain in **Fig. 2c**. The correlation between AFE/FE strain and $\Delta E$ is reaffirmed, and all 10 compositions tested exhibited $\eta \geq 93.0\%$. Compositions 1 through 5 display $\Delta E < 1$ kV/cm, $\eta > 96\%$, and $W_{rec} \geq 3.0$ J/cm$^3$. Two of these compositions: $(Pb_{0.875}Ba_{0.05}Sr_{0.03}La_{0.03})(Zr_{0.58}Sn_{0.36}Ti_{0.06})O_3$ (#3) and $(Pb_{0.865}Ba_{0.06}Sr_{0.03}La_{0.03})(Zr_{0.58}Sn_{0.34}Ti_{0.08})O_3$ (#4) have an efficiency of 97.4% and 97.6%, respectively. Composition 6, $(Pb_{0.905}Ba_{0.03}Sr_{0.02}La_{0.03})(Zr_{0.58}Sn_{0.34}Ti_{0.08})O_3$ has a slightly higher strain (0.537%) and a $\Delta E$ = 3.2 kV/cm. Its efficiency is still high at 95.7%. The *P vs. E* curves under unipolar fields of these six compositions are displayed in **Fig. S4**. The experimental validations shown in **Fig. S2** and **Fig. 2c** demonstrate that the geometric nonlinear theory is successful in guiding the discovery of AFE ceramics for energy-efficient capacitors.

The DFT calculations of the low AFE/FE mismatch strain and the experimental validation of $\Delta E < 1$ kV/cm in (Pb,Sr,Ba,La)(Zr,Sn,Ti)$O_3$ compositions suggests that this solid solution

with Sr and Ba co-substitutions is promising for reaching a near-perfect energy efficiency. We used these predicted and validated compositions as starting points and broadened our composition spread by implementing an accelerated synthesis approach and employed $\Delta E$ as a high-throughput screening tool to generate a library of nearly 500 compositions (see details in **Fig. S5**). We focused on compositions in the highlighted region in **Fig. 2a** for further measurements of $\eta$ and $W_{rec}$. The results of these measurements are illustrated in the form of heat maps, shown in **Fig. 3**. Overall, the heat map of $\eta$ is in agreement with that of AFE/FE strain in **Fig. 2b**; the heat map of $W_{rec}$ is in agreement those of FE-cell angle and AFE stability in **Fig. 2b**. Specifically, we found that Sn is beneficial to reducing $\Delta E$ and enhancing $\eta$. Increase in Ti content leads to a lower breakdown strength and a lower $E_F$ (hence, a lower $W_{rec}$); also a slight decrease in $\eta$. Substitution of Pb with Sr and Ba considerably reduces $\Delta E$ and improves $\eta$. However, their contents beyond 5 at.% lead to drop in $W_{rec}$ due to reduction in $P_{max}$ and drop in $\eta$ owing to rise in $P_r$.

Our accelerated materials synthesis and screening of 500+ compositions (3 repeats per composition) successfully identified the best AFE composition SB5408, as presented in **Fig. 1**. Near this composition, another 3 compositions are also discovered to have an $\eta$ of 96.8%, 97.7%, and 98.3%, respectively, with a $W_{rec}$ around 3.0 J/cm$^3$, as shown in **Fig. S6**. This attribute is important for future large-scale materials production as composition control is not super stringent. The two best performing compositions, SB5408 and SB5407, with $\eta > 98.0\%$ are marked by yellow stars in the left panel of **Fig. 3**.

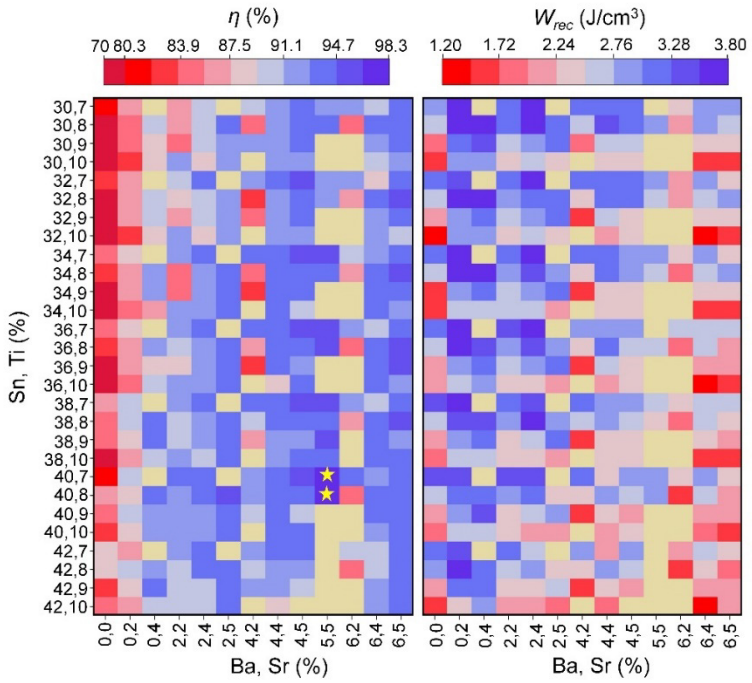


**Figure 3.** Combinatorial synthesis of (Pb,Sr,Ba,La)(Zr,Sn,Ti)$O_3$ ceramics with compositions (La = 2 at.%) near those discovered by theory. **Left.** The heat map of experimentally measured $\eta$. The discovered compositions with $\eta$ > 98.0% are marked by the yellow stars. **Right.** The heat map of experimentally measured $W_{rec}$. The boxes shaded in yellow represent the compositions that exhibited very poor breakdown strength. $W_{rec}$ and $\eta$ are quantified from unipolar *P vs. E* curves.

We then characterized the structure and properties of the best composition SB5408. **Figure 4a** illustrates the X-ray diffraction spectra recorded at room temperature (top panel) and 60 K (bottom panel). The room temperature structure appears to be a single-phase perovskite with tetragonal distortion, consistent with the structure of $PbZrO_3$-based AFE ceramics commonly reported in literature.[9,21,39] When cooled to low temperature (60 K), the SB5408 ceramic adopts a monoclinic crystal structure (space group *Pm*) based on the full profile refinement. The temperature-driven structural evolution of SB5408 during warming up from 60 K to room temperature is illustrated in the contour plots in **Fig. 4b** and **c**. The X-ray diffraction measurements indicate a gradual structural change, and the ceramic exists as a mixture of monoclinic and tetragonal phases over a temperature range of 180 - 220 K. The $(\bar{1}03)_M$ peak is observed to undergo an accelerated shift toward lower angles near 220 K, whilst the $(\bar{3}01)_M$ peak increases slightly in its intensity but does not shift in position. The intensity drop of the $(103)_T$ reflection above 240 K is a direct result of separating from $K\alpha_2$ of

the $(301)_T$ reflection which coincides with the $(\bar{1}03)_M$ reflection. A similar trend is seen in the $(121)_M$ and $(112)_M$ peaks, which later merge into the $(211)_T$ and $(112)_T$ peaks, respectively. To avoid ambiguity due to the overlapping $(211)_T$ and $(112)_T$ peaks, we choose to fit the line profile of (222) peak with the Lorentzian function. The full width at half maximum (FWHM) (222) is apparently larger at temperatures below 220 K (**Fig. S7)**, which can be attributed to the dominant phase with the monoclinic symmetry at low temperatures.

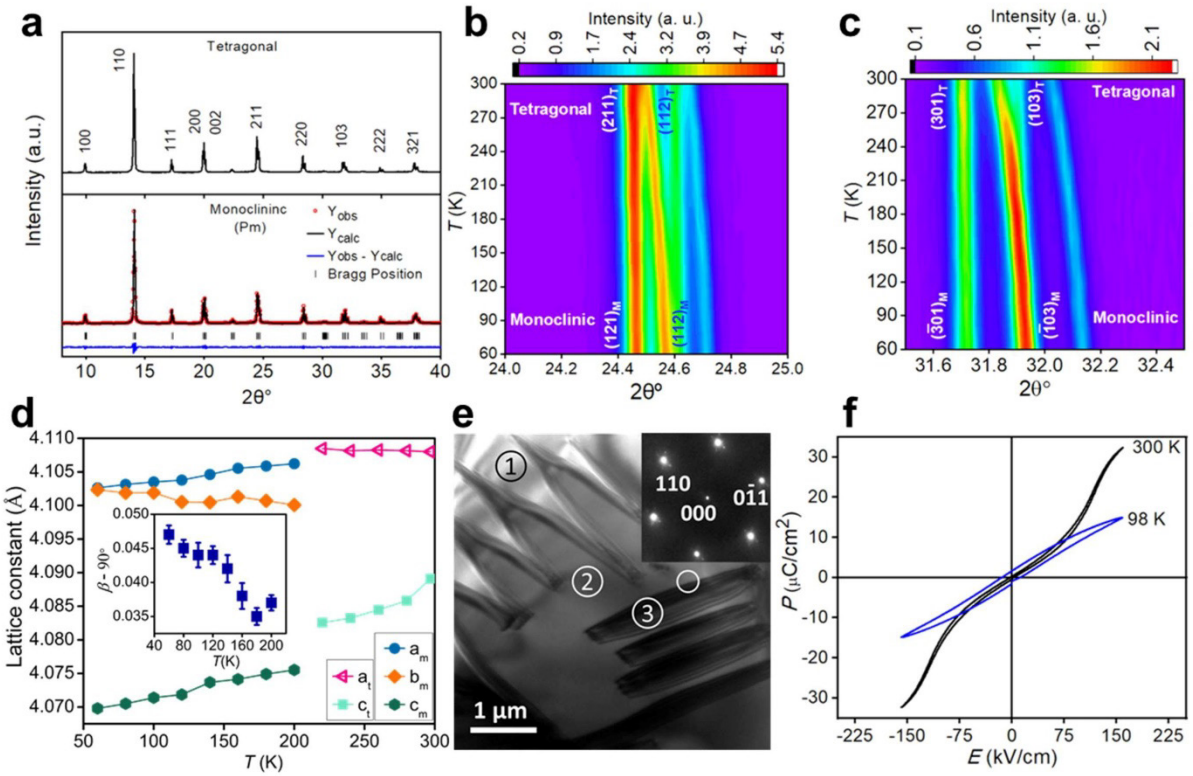


**Figure 4.** Structure and electrical properties of SB5408 ceramic. **a.** X-ray diffraction analysis at room temperature (top panel) and 60 K (bottom panel). **b, c.** Contour plots of selected X-ray diffraction peaks to illustrate the evolution of their position and intensity during heating from 60 K to room temperature. **d.** Lattice parameters extracted from X-ray diffraction analysis (The error bars are smaller than the symbols). The inset shows the evolution of the monoclinic angle $\beta$ with temperature. **e.** Transmission electron microscopy analysis of the microstructure; the electron diffraction pattern of <$\bar{1}11$> zone-axis in the inset is obtained from the circled area. **f.** Bipolar $P$ vs. $E$ loops at 98K and 300K.

The temperature evolution of the unit-cell lattice parameters, obtained from analysis of the X-ray powder diffraction data, is shown in **Fig. 4d**. The discontinuous change in lattice parameters, along with the coexistence of two phases over a temperature range, indicates the monoclinic – tetragonal phase transition in SB5408 is first-order in nature. The microstructure of the SB5408 ceramic at room temperature is analyzed with transmission electron

microscopy (**Fig. 4e**). The bright field micrograph, recorded along the <$\bar{1}$11> zone-axis of the grain, consists of three sets of domains, labeled as 1, 2, and 3. The electron diffraction pattern shown in the inset was obtained from the circled area. There are two sets of satellite spots in the diffraction pattern, confirming the presence of incommensurate modulations in the $AFE_T$ phase of SB5408 at room temperature. As these modulations originate primarily from cation displacements,[16,40,41] the low intensity of these satellite spots in SB5408 suggests there might be a fraction of volume that contains cation displacements and at a smaller amplitude.

To corroborate the temperature-dependent X-ray diffraction findings, we measured the *P* vs. *E* loops under bipolar fields in the temperature range of 98 - 300K (**Fig. 4f**). At 98K, the SB5408 ceramic displays a single slim *P* vs. *E* loop. Upon increase in temperature near 170 K, the *P* vs. *E* loop begins to convert into double hysteresis loops (not shown here), indicating the transition to the AFE phase. Hence, we suggest the low-temperature monoclinic phase revealed by X-ray diffraction is a FE phase. We speculate that the small electric hysteresis in the FE phase for polarization reversal is inherited from the near-zero $\Delta E$ in the AFE–FE transition.

Results from additional experimental measurements on SB5408 are displayed in **Fig. S8**. The dielectric constant vs. temperature curve exhibits a broad hump around 180 K, peaks at 411 K, exhibits another hump at 478 K. According to our X-ray diffraction analysis results and the phase transition sequence in previous reports[16,41] on other $PbZrO_3$-based AFE ceramics, SB5408 is monoclinic FE below 180 K, tetragonal AFE between 180 and 411 K, multicell cubic paraelectric between 411 and 478 K, and single-cell cubic paraelectric above 478 K. Interestingly, dielectric constant curves measured upon heating and cooling overlap each other, revealing a near-zero thermal hysteresis for the FE–AFE phase transition (**Fig. S8a**), even though it is a first-order transition. This observation is in sharp contrast to other $PbZrO_3$-based AFE ceramics with a large $\Delta E$, where a huge thermal hysteresis of 51 K was

observed.[42] The result suggests that minimized AFE/FE interfacial mismatch strain enhances the reversibility of the AFE–FE phase transition triggered by both electric field and temperature. The low-temperature monoclinic phase exhibits an apparent frequency dependence of the dielectric constant (**Fig. S8b**). The polarization measurement indicates *P* vs. *E* double hysteresis loops remain at least up to 367 K (**Fig. S8c**), supporting the AFE nature between 180 and 411 K. The comparison of the unipolar *P* vs. *E* loops at initial stage and after 79.5 millions cycles is displayed in **Fig. S8d**. The portion of the curves below 120 kV/cm remains unchanged, while minor degradation in $P_{max}$ is seen in the induced FE phase. In SB5408, the compatible AFE/FE interface ensures excellent reversibility of the AFE–FE transition, achieves record-high energy efficiency, and extends the charge-discharge lifetime.

Our approach to realize ultra-high energy efficiency by designing compatible AFE/FE interfaces has not yet been reported previously in AFE ceramics. A most recent approach is to introduce aliovalent cations that lead to the so-called "*relaxor antiferroelectric*" behavior by randomizing the local fields and disrupting long-range AFE order. For example, $Bi^{3+}$, $Zn^{2+}$, and $Nb^{5+}$ , in the nominal form of $Bi(Zn_{2/3}Nb_{1/3})O_3$, were introduced to a $(Pb,La)(Zr,Sn,Ti)O_3$ AFE ceramic and an efficiency of 95.6% was achieved.[28] By analyzing the temperature-dependent dielectric constant in the paraelectric phase of SB5408, our ceramic is not likely to be a relaxor AFE. The dielectric data of SB5408 is fitted with the expression,[43] $\frac{\varepsilon_{m,r}}{\varepsilon_r} = 1 + \frac{(T-T_m)^\gamma}{2\delta^2}$, where $\gamma$ is the degree of dielectric relaxation, which equals to 1 for a normal AFE and 2 for an ideal relaxor AFE,[28] $\delta$ is the degree of diffuseness of the transition, $\varepsilon_{m,r}$ is the maximum value of the dielectric constant, and $T_m$ is the temperature where the dielectric constant reaches $\varepsilon_{m,r}$. The values of $\gamma$ and $\delta$ for SB5408 are determined to be 1.14 and 13.5, respectively. In contrast, the $Bi(Zn_{2/3}Nb_{1/3})O_3$-modified $(Pb,La)(Zr,Sn,Ti)O_3$ relaxor AFE ceramic has the values of 1.65 and 51.8, respectively,[28] much higher than those of SB5408.

We further assess the compatibility indicator, the eigenvalue $\lambda_2$ of the AFE–FE transition stretch tensor, in two situations. First, the lattice parameters of the monoclinic FE phase are extrapolated to room temperature to match the lattice parameters of the tetragonal AFE phase. The $\lambda_2$ is calculated to be 0.9988. This value is very close to unity, verifying that the AFE/FE interface at room-temperature is highly compatible and supporting the excellent reversibility of the electric field-induced AFE–FE transition at room temperature. Second, the lattice parameters of the tetragonal AFE phase are extrapolated to 200 K to match the lattice parameters of the monoclinic FE phase. The $\lambda_2$ is calculated to be 0.9979. This value is also close to unity, suggests that the AFE/FE interface at 200 K is highly compatible. The result supports the good reversibility of the temperature-induced AFE–FE transition in this temperature range.

## 3. Conclusions

In summary, the geometric nonlinear theory of martensitic transitions is demonstrated to guide the discovery of $PbZrO_3$-based antiferroelectric ceramics with a world-record charge-discharge energy efficiency. First, DFT results are conducted to identify promising compositions with a small AFE/FE interfacial mismatch strain, a large polarization in the FE phase, and an appropriate AFE phase stability. After experimental validation, high-throughput synthesis is performed to fabricate ceramics with compositions in the vicinity of the best compositions. Then, electrical properties screening leads to the discovery of four compositions with near-perfect energy efficiency (~98%). These ceramics exhibit a recoverable energy density of ~3.0 J/cm$^3$ at an applied field of ~220 kV/cm. Most importantly, the fatigue life of the AFE capacitor reaches 79.5 million charge-discharge cycles, an enhancement of 80 times over AFE ceramics with large electric hysteresis. The established methodology can be applied to the discovery of other functional ceramics, such as Pb-free AFE ceramics with ultrahigh energy efficiency.

## Methods and Materials

*DFT calculations and compatibility assessment.* Details are provided in the Supplementary Information.

*Materials synthesis.* (Pb,Sr,Ba,La)(Zr,Sn,Ti)$O_3$ ceramics were prepared by the solid-state reaction. PbO, $ZrO_2$, $TiO_2$, $La_2O_3$, $SnO_2$, $SrCO_3$, and $BaCO_3$ powders with purity higher than 99.9% were weighed and mixed according to the chemical formula. Excess 4% PbO was added to compensate the loss of Pb during sintering. Raw powders were ball-milled for 6 hours and dried at 80 °C under a vacuum oven. Dried powder was then pressed into 1-inch disks and calcined at 935 °C for 4 hours. The calcined powders were ball-milled again for 6 hours, dried, mixed with 5 wt% PVA binder, and then pressed into pellets of 10 mm in diameter. Finally, the binder was burnt out at 600 °C for 3 hours and the pellets were sintered at 1350 °C for 3 hours under the double crucible arrangement. As depicted in **Fig. S5**, a 6-channel auto powder dispenser and a 32-channel mixing and milling machine were used to increase throughput of material synthesis. In addition, 18 compositions in a 2-layer arrangement were calcined and sintered in each run. The experimental setup is capable of fabricating 50 compositions per week.

*Electrical properties characterization.* Sintered ceramic pellets were thinned and polished to the thickness of 0.2-0.25 mm. Silver films with a diameter of 4 mm were sputtered as electrodes. The room temperature *P* vs. *E* hysteresis loops were measured using a standardized ferroelectric test system (Precision LC II, Radiant Technologies) under unipolar fields at a frequency of 1 Hz. For the fatigue test, Ag/Pd bilayer film electrodes with a diameter of 2 mm were used, and the test was carried out under unipolar fields at 25 Hz at room temperature. For the low-temperature bipolar *P* vs. *E* hysteresis loop measurement, the sample was immersed in an electrical fluid and the temperature was controlled with a Delta

9023 environmental chamber. The dielectric constant vs. temperature measurements were conducted using a Novocontrol system at a heating/cooling rate of 1 K/min at frequencies of 0.1, 1, 10, and 100 kHz.

*X-ray diffraction.* The temperature dependent X-ray diffraction analysis was carried out on a modified Rigaku TTRAX system equipped with a θ/2θ wide-angle goniometer and an 18-kW rotating anode X-ray source. The instrument employs Mo Kα radiation in the Bragg–Brentano geometry, the slow scanning speed (time/step: 3 s per 0.001°) was set to clearly observe the diffraction pattern in the 2θ range of 8 - 40°. Sintered pellets were crushed into powder for the measurement and Rietveld refinement was carried out with the Full Prof software package. The detailed description of the system and the sample preparation procedure can be found elsewhere.[44]

*Transmission electron microscopy.* Specimens were prepared with procedures involving polishing, ultrasonic cutting, dimpling, and argon ion mill. To mitigate the charging effect, a thin layer of approximately 10 nm carbon was deposited onto the specimen. Bright field micrographs and select-area electron diffraction patterns were captured using the FEI Titan Themis microscope.

## Supplementary Information

Supplementary Information is available from the Wiley Online Library or from the author.


## Acknowledgements

This material is based upon work supported by the U.S. Department of Energy's Office of Energy Efficiency and Renewable Energy (EERE) under the Advanced Manufacturing Office (AMO) Award Number DE-EE0009105.

## Conflict of Interest

The authors declare no conflict of interest.

## Data Availability Statement

The data that support the findings of this study are available from the corresponding author upon reasonable request.

Received: ((will be filled in by the editorial staff))
Revised: ((will be filled in by the editorial staff))
Published online: ((will be filled in by the editorial staff))

[1] I. Husain, M.S. Islam, E. Gurpinar, W. Yu, L. Xue, R. Sahu, *Proc. IEEE* **2021**, *109(6)*, 1039.

[2] M.J. Pan, C.A. Randall, *IEEE Electr. Insul. Mag.* **2010**, *26*, 44.

[3] G. Wang, Z. Lu, Y. Li, L. Li, H. Ji, A. Feteira, D. Zhou, D. Wang, S.J. Zhang, I.M. Reaney, *Chem. Rev.* **2021**, *121*, 6124.

[4] S. Kwon, W. Hackenberger, E. Alberta, E. Furman, M. Lanagan, *IEEE Electr. Insul. Mag.* **2011**, *27*, 43.

[5] J.P. Dougherty, U.S. Patent, **1996**, 5,545,184.

[6] H. Wang, Y. Liu, T. Yang, S. Zhang, *Adv. Funct. Mater.* **2019**, *29*,1807321.

[7] X. Liu, Y. Li, X. Hao, *J. Mater. Chem. A* **2019**, *7*, 11858.

[8] X. Liu, J. Zhu, Y. Li, T. Yang, X. Hao, W. Gong, *Chem. Eng. J.* **2022**, *446*, 136729.

[9] X. Wang, Q. Zhu, H. Sun, M. Wang, R. Xu, Y. Feng, Z. Li, X. Wei, Z. Xu, *J. Euro. Ceram. Soc.* **2023**, *43*, 4051.

[10] G. Ge, C. Shi, C. Chen, Y. Shi, F. Yan, H. Bai, J. Yang, J. Lin, B. Shen, J. Zhai, *Adv. Mater.* **2022**, *34*, 2201333.

[11] W. Pan, Q. Zhang, A. Bhalla, and L.E. Cross, *J. Am. Ceram. Soc.* **1989**, *72*, 571.

[12] S.I. Shkuratov, J. Baird, V.G. Antipov, S. Zhang, J.B. Chase, *Adv. Mater.* **2019**, *31*, 1904819.

[13] https://en.tdk.eu/tdk-en/1054426/products/product-catalog/ceramic-capacitors/ceralink-capacitors

[14] L. Zhou, R. Z. Zuo, G. Rixecker, A. Zimmermann, T. Utschig, F. Aldinger, *J. Appl. Phys.* **2006**, *99*, 044102.

[15] P. Mohapatra, D. Johnson, J. Cui, X. Tan, *J. Mater. Chem. C* **2021**, *9*, 15542.

[16] D. Viehland, D. Forst, Z. Xu, J.F. Li, *J. Am. Ceram. Soc.* **1995**, *78*, 2101.

[17] X. Tan, C. Ma, J. Frederick, S. Beckman, K.G. Webber, *J. Am. Ceram. Soc.* **2011**, *94*, 4091.

[18] Z. Liu, X. Chen, W. Peng, C. Xu, X. Dong, F. Cao, G. Wang, *Appl. Phys. Lett.* **2015**, *106*, 262901.

[19] G. Zhang, D. Zhu, X. Zhang, L. Zhang, J. Yi, B. Xie, Y. Zeng, Q. Li, Q. Wang, S. Jiang, *J. Am. Ceram. Soc.* **2015**, *98*, 1175.

[20] Z. Yang, H. Du, L. Jin, D. Poelman, *J. Mater. Chem. A* **2021**, *9*, 18026.

[21] S.E. Park, K. Markowski, S. Yoshikawa, L.E. Cross, *J. Am. Ceram. Soc.* **1997**, *80*, 407.

[22] M.J. Pan, S.E. Park, K. Markowski, W.S. Hackenberger, S. Yoshikawa, L.E. Cross, *Ferroelectrics* **1998**, *215*, 153.

[23] J. Wang, T. Yang, S. Chen, G. Li, *Mater. Res. Bull.* **2013**, *48*, 3847.

[24] Y. Li, J. Gao, T. Yang, *J. Phys. Chem. Solids* **2023**, *172*, 111046.

[25] R. Xu, Z. Xu, Y. Feng, J. Tian, D. Huang, *Ceram. Int.* **2016**, *42*, 12875.

[26] R. Xu, B. Li, J. Tian, Z. Xu, Y. Feng, X. Wei, D. Huang, L. Yang, *Appl. Phys. Lett.* **2017**, *110*, 142904.

[27] P. Liu, G. Zhu, Q. Zhang, H. Zhang, *Ceram. Int.* **2022**, *48*, 16933.

[28] P. Mohapatra, Z. Fan, J. Cui, X. Tan, *J. Euro. Ceram. Soc.* **2019**, *39*, 4735.

[29] B.Z. Liu, X.C. Tian, L. Zhou, X. Tan, *Phys. Rev. Mater.* **2020**, *4*, 104417.

[30] K. Bhattacharya, S. Conti, G. Zanzotto, J. Zimmer, *Nature* **2004**, *428*, 55.

[31] R.D. James, Z. Zhang, in *Magnetism and Structure in Functional Materials*. A. Planes, L. Manosa, and A. Saxena eds., Springer (Berlin), **2005**, p. 159-175.

[32] X. Chen, V. Srivastava, V. Dabade, and R.D. James, *J. Mech. Phys. Solids* **2013**, *61*, 2566.

[33] J. Cui, Y.S. Chu, O.O. Famodu, Y. Furuya, J. Hattrick-Simpers, R.D. James, A. Ludwig, S. Thienhaus, M. Wuttig, Z. Zhang, I. Takeuchi, *Nat. Mater.* **2006**, *5*, 286.

[34] Y. Song, X. Chen, V. Dabade, T.W. Shield, and R.D. James, *Nature* **2013**, *502*, 85.

[35] C. Chluba, W. Ge, R.L. de Miranda, J. Strobel, L. Kienle, E. Quandt, M. Wuttig, *Science* **2015**, *348*, 1004.

[36] M. Wegner, H. Gu, R.D. James, E. Quandt, *Sci. Rep.* **2020**, *10*, 3496.

[37] C. Zhang, Z. Zhu, J. Choi, J. Kim, X. Chen, *Appl. Phys. Lett.* **2021**, *119*, 082902.

[38] E.L. Pang, G.B. Olson, C.A. Schuh, *Nature* **2022**, *610*, 491.

[39] Q. Zhang, X. Liu, Y.Zhang, X. Song, J. Zhu, I. Baturin, J. Chen, *Ceram. Int.* **2015**, *41*, 3030.

[40] D. Viehland, *Phys. Rev. B* **1995**, *52*, 778.

[41] H. He, X. Tan, *Phys. Rev. B* **2005**, *72*, 024102.

[42] H. Guo, X. Tan, *Phys. Rev. B* **2015**, *91*, 144104.

[43] K. Uchino, S. Nomura, *Ferroelectric Lett.* **1982**, *44*, 55.

[44] A. P. Holm, V. K. Pecharsky, K. A. Gschneidner Jr., R. Rink, M. N. Jirmanus, *Rev. Sci. Instr.* **2004**, *75*, 1081.

**The table of contents entry:**

**A near-perfect charge-discharge energy efficiency, 98.2%**, is observed in a $PbZrO_3$-based antiferroelectric ceramic. The compositions with such compatible antiferroelectric – ferroelectric phase transitions are discovered by theory-guided high-throughput synthesis. The almost eliminated electric hysteresis is a result of minimized lattice mismatch strain at the interface during phase transition. The highly energy-efficient capacitor also exhibits 80 times enhancement in service lifetime.

**Keywords:** antiferroelectric-ferroelectric phase transition, geometric nonlinear theory of martensite, lattice mismatch strain, electric hysteresis, energy efficiency, $PbZrO_3$-based oxides

**Authors:** Anand P.S. Gaur, Renu Choudhary, Binzhi Liu, Yaroslav Mudryk, Duane Johnson, Jun Cui and Xiaoli Tan*

**Title: Antiferroelectric Ceramics for Energy-Efficient Capacitors by Theory-Guided Discovery**
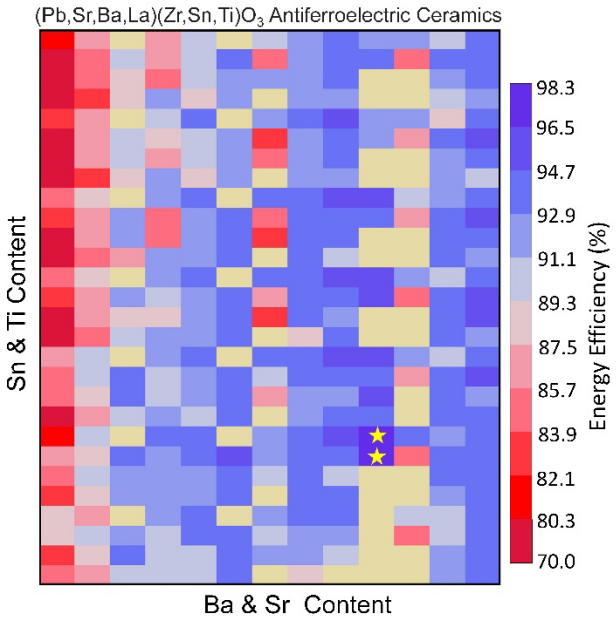
ToC figure